JACS
JOURNAL OF THE AMERICAN CHEMICAL SOCIETY
Article
Cite This: J. Am. Chem. Soc. 2018, 140, 5290−5299
pubs.acs.org/JACS

Phenothiazine Radical Cation Excited States as Super-oxidants for Energy-Demanding Reactions

Joseph A. Christensen,[†] Brian T. Phelan,[†] Subhajyoti Chaudhuri,[‡] Atanu Acharya,[‡] Victor S. Batista,[‡] and Michael R. Wasielewski*[,†]

[†]Department of Chemistry and Argonne−Northwestern Solar Energy Research (ANSER) Center, Northwestern University, Evanston, Illinois 60208-3113, United States

[‡]Department of Chemistry and Argonne−Northwestern Solar Energy Research (ANSER) Center, Yale University, New Haven, Connecticut 06520, United States

Supporting Information

ABSTRACT: We demonstrate that the 10-phenyl-10*H*-phenothiazine radical cation ($PTZ^{+\bullet}$) has a manifold of excited doublet states accessible using visible and near-infrared light that can serve as super-photooxidants with excited-state potentials is excess of +2.1 V vs SCE to power energy demanding oxidation reactions. Photoexcitation of $PTZ^{+\bullet}$ in CH_3CN with a 517 nm laser pulse populates a D_n electronically excited doublet state that decays first to the unrelaxed lowest electronic excited state, D_1' (τ < 0.3 ps), followed by relaxation to D_1 (τ = 10.9 ± 0.4 ps), which finally decays to D_0 (τ = 32.3 ± 0.8 ps). D_1' can also be populated directly using a lower energy 900 nm laser pulse, which results in a longer $D_1'\rightarrow D_1$ relaxation time (τ = 19 ± 2 ps). To probe the oxidative power of $PTZ^{+\bullet}$ photoexcited doublet states, $PTZ^{+\bullet}$ was covalently linked to each of three hole acceptors, perylene (Per), 9,10-diphenylanthracene (DPA), and 10-phenyl-9-anthracenecarbonitrile (ACN), which have oxidation potentials of 1.04, 1.27, and 1.6 V vs SCE, respectively. In all three cases, photoexcitation wavelength dependent ultrafast hole transfer occurs from D_n, D_1', or D_1 of $PTZ^{+\bullet}$ to Per, DPA, and ACN. The ability to take advantage of the additional oxidative power provided by the upper excited doublet states of $PTZ^{+\bullet}$ will enable applications using this chromophore as a super-oxidant for energy-demanding reactions.

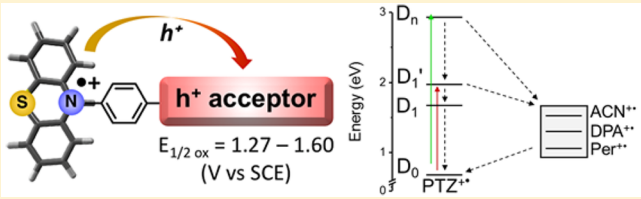

INTRODUCTION

Solar-powered water splitting represents one potential solution to provide for the ever-growing global energy demand without generating greenhouse gas emissions.[1] Many challenges must be overcome for water splitting to be a viable technology for grid scale energy production,[2] and one underexplored area is the development of chromophores capable of acting as photo-driven super-oxidants to power water oxidation catalysis with low-energy visible and/or near-infrared (NIR) solar photons. Green plant and cyanobacterial photosynthesis use two tandem photosystems to achieve the potentials necessary to oxidize water and drive carbon dioxide reduction using low-energy photons.[3] Recent studies have focused on mimicking this behavior in dual electron donor−acceptor systems.[4−8] Radical ion excited doublet (S = 1/2) states provide another approach to using low-energy photons to drive energy-demanding reactions. The pioneering studies of Fox[9−11] and Vauthey[12−17] on the excited states of a variety of radical ions found that most of these species have lifetimes that are very short as a result of their low-lying excited-state energies (energy gap law),[18] and/or the presence of conical intersections connecting their ground and excited states.[19] This makes it difficult to use many radical ion excited states as powerful reductants or oxidants because the desired charge-transfer reactions cannot out-compete their excited-state decay. Detailed characterization of the photophysics of organic radical ion excited states is therefore necessary to optimize their use as photosensitizers.

We have investigated the excited states of stable arylene imide and diimide radical anions,[20] and have discovered that most of these radical anions have lifetimes τ > 100 ps, making their excited states potentially useful as powerful electron donors. In our earlier studies, we photoexcited the donor in a donor−acceptor system in which naphthalene diimide (NDI) served as the acceptor resulting in rapid reduction of NDI to $NDI^{-\bullet}$. Selective secondary photoexcitation of $NDI^{-\bullet}$ to its excited doublet state provided the extra energy needed to transfer an electron from $^2{*}NDI^{-\bullet}$ to a more difficult to reduce pyromellitimide acceptor covalently bound to the donor−acceptor pair.[21,22] While these original experiments were designed to illustrate all-optical molecular logic gates, it has recently become clear that radical anion excited states can be used as electron donors to a variety of substrates.[23−30] We have subsequently extended our work on radical anion excited states by examining spin coherence in such systems,[31,32] and by using their super-reductant properties to drive carbon dioxide reduction catalysts.[33−36]

Received: February 12, 2018
Published: March 28, 2018

DOI: 10.1021/jacs.8b01778
J. Am. Chem. Soc. 2018, 140, 5290−5299

In the work presented here, we investigate the possibility that radical cations can serve as super-oxidants. Because open-shell cationic organic chromophores typically have $D_n \leftarrow D_0$ electronic transitions in the visible and NIR regions of the electromagnetic spectrum,[37−39] these species are of particular interest as photosensitizers for solar energy capture and conversion. The photophysics of open-shell organic molecules is not as well studied as their closed-shell counterparts, and the dynamics of intramolecular charge transfer involving doublet excited states have only been studied in a small number of systems, nearly all of which are based on electron transfer from photoexcited organic radical anions.[28,30]

We sought to identify a stable organic radical cation that absorbs in the visible or NIR spectral region whose doublet excited state has sufficient oxidizing power to serve as a super-oxidant for solar energy purposes.[2] Phenothiazines have been widely employed as electron donors in photoinduced charge-transfer reactions for applications including, but not limited to, chemical sensing,[40] dye-sensitized solar cells,[41,42] quantum-dot oxidation,[43] organic light-emitting diodes,[44] and molecular switches.[45] They are suitable for these purposes because of the remarkable stability of their radical cations and their moderate one-electron oxidation potentials.[46] For example, the 10-phenyl-10*H*-phenothiazine radical cation ($PTZ^{+\bullet}$) has electronic absorption bands in the visible and NIR regions, and its properties have been studied by steady-state optical absorbance and electron paramagnetic resonance (EPR) spectroscopies;[47−49] but despite its ubiquity, the dynamics of its doublet electronic excited states have not yet been characterized. In this work, we employed ultrafast transient absorption spectroscopy and femtosecond stimulated Raman spectroscopy (FSRS),[50] to characterize the $PTZ^{+\bullet}$ excited doublet-state deactivation dynamics after visible and NIR excitation, and have used time-dependent density functional theory (TDDFT) calculations to interpret the results. In addition, three donor−acceptor dyads (Scheme 1) were prepared to study the effect of reaction free energy on the rate and yield of hole transfer from the $PTZ^{+\bullet}$ excited doublet states. The excitation-energy-dependent $PTZ^{+\bullet}$ excited-state dynamics resulted in surprising charge-transfer dynamics in the donor−acceptor dyads. These results demonstrate that the electronically excited doublet states of $PTZ^{+\bullet}$ can provide oxidizing potentials in excess of 2.1 V vs SCE to carry out difficult oxidation reactions, which will allow for the design of supramolecular photosensitizer−catalyst assemblies in which the catalyst requires strongly oxidizing potentials.

Scheme 1. (A) Structures of PTZ and Donor−Acceptor Dyads and (B) Synthesis of $PTZ^{\bullet+}$-R

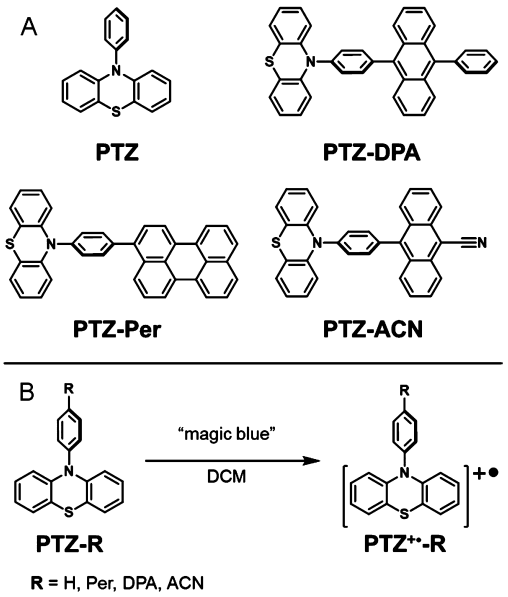

■ EXPERIMENTAL SECTION

Synthesis. The molecules studied are shown in Scheme 1 and their synthesis and characterization is described in detail in the Supporting Information. Briefly, PTZ and PTZ-9,10-diphenylanthracene (PTZ-DPA) were prepared as described previously.[51,52] PTZ-perylene (PTZ-Per) and PTZ-9-anthracenecarbonitrile (PTZ-ACN) were prepared by Suzuki−Miyaura cross-coupling reactions between components whose preparation has been described previously.[51,53,54] The radical cations were prepared by mixing solutions of the phenothiazine-containing molecules (1 mL, 1.0 mM, CH_2Cl_2) with a solution of tris(4-bromophenyl)ammoniumyl hexachloroantimonate ("magic blue") oxidant (0.5 mL, 1.4 mM, CH_2Cl_2). Upon the addition of the oxidant, the solutions turned red immediately. For optical measurements in acetonitrile (CH_3CN), the CH_2Cl_2 was removed under reduced pressure, and then the samples were re-dissolved in CH_3CN, filtered, and diluted with CH_3CN to an appropriate optical density.

Steady-State Optical Spectroscopy. UV−visible (λ = 300−1100 nm) steady-state absorption spectra were recorded at room temperature using a Shimadzu UV-1800 spectrometer, and the UV−visible−NIR (λ = 300−2500 nm) spectrum was recorded at room temperature using a Shimadzu UV-3600 spectrometer. The NIR emission spectrum was recorded at room temperature using a Horiba Nanolog fluorimeter equipped with a Xe lamp excitation source and an LN_2-cooled InGaAs array detector. The sample was prepared with an absorbance at λ = 515 (880) nm of 0.8 (0.15) and was excited at λ = 515 nm and the spectra represent the average of five 120 s exposures.

Electrochemistry. Electrochemical measurements were performed on a CH Instruments 750E electrochemical workstation. Measurements were made using a 1.0 mm diameter platinum working electrode, a platinum wire auxiliary electrode, and a silver wire reference electrode in 0.1 M solutions of tetra-*n*-butylammonium hexafluorophosphate ($TBAPF_6$) in CH_3CN purged with argon. The ferrocene/ferrocenium couple was used as an internal standard (0.4 V vs SCE in CH_3CN).[55]

Transient Absorption Spectroscopy. Femtosecond transient absorption spectroscopy (fsTA) experiments were performed using a regeneratively amplified Ti:sapphire laser system (Tsunami oscillator/Spitfire Pro amplifier, Spectra-Physics) as previously described[56] with the following modification to the probe generation and detection. The UV−vis continuum probe ($\lambda \approx$ 330−800 nm) was generated by focusing the λ = 827 nm fundamental (100 fs, 2 μJ) into a 3 mm CaF_2 crystal cut along the ⟨001⟩ axis (Newlight Photonics Inc.). The CaF_2 crystal was translated vertically 7.5 mm at 1.5 mm/s using a linear actuator (LAC10A-T4/X-MCB1, Zaber Technologies Inc.) to minimize the effects of optical damage by the fundamental. The NIR continuum probe ($\lambda \approx$ 850−1600) was generated by focusing the λ = 827 nm fundamental (100 fs, 3 μJ) into a 10 mm proprietary crystal (Ultrafast Systems, LLC). The probe pulse was split prior to interaction with the sample to provide signal and reference probe pulses which were detected with a customized Helios spectrometer and Helios software (Ultrafast Systems, LLC). The samples were irradiated at λ_{ex} = 517 or 900 nm with ∼110 fs, 1 μJ pulses with randomized polarization (DPU-25-A, Thorlabs, Inc.) to suppress observation of rotational dynamics. The λ_{ex} = 517 nm excitation pulse was generated with a home-built optical parametric amplifier,[56] and the λ_{ex} = 900 nm excitation pulse was generated with a commercial non-collinear optical parametric amplifier (TOPAS-White, Light Conversion). Transient spectra were acquired with three second averaging at each time delay point. The instrument response was about 300 fs.

DOI: 10.1021/jacs.8b01778
J. Am. Chem. Soc. 2018, 140, 5290−5299

The fsTA data were corrected for group delay dispersion, or chirp, and scattered light prior to the kinetic analysis using Surface Xplorer (Ultrafast Systems, LLC). The kinetic analysis was performed using home-written programs in MATLAB[57] and was based on a global fit to selected single-wavelength kinetics. The time resolution is given as w = 300 fs (full width at half-maximum); the assumption of a uniform instrument response across the frequency domain and a fixed time-zero are implicit to global analysis. The data were globally fit either to specified kinetic models or a sum of exponentials. The data set was then deconvoluted with the resultant populations or amplitudes to reconstruct the species-associated or decay-associated spectra. Detailed descriptions of the kinetic models can be found in the Supporting Information.

Femtosecond Stimulated Raman Spectroscopy. Steady-state and time-resolved femtosecond stimulated Raman spectroscopy (FSRS) experiments were performed using a 1 kHz Ti:sapphire system (MaiTai oscillator/Spitfire Pro Amplifier, Spectra-Physics) described previously.[53] Briefly, the probe pulse (370−800 nm) was generated by focusing a portion of the fundamental (<100 fs, 1 μJ) into a 1:1 H_2O:D_2O mixture in a 5 mm quartz cuvette. The Raman pump pulse was generated using a second harmonic bandwidth compressor (SHBC, Light Conversion) coupled to a commercial optical parametric amplifier (TOPAS-400-WL, Light Conversion) and was centered at 540 and 400 nm (∼1 ps, 0.7 μJ) for the steady-state FSRS and time-resolved FSRS experiments, respectively. The actinic pump pulse used in the time-resolved FSRS experiment was generated using a commercial optical parametric amplifier (TOPAS-C, Light Conversion) and was centered at 515 nm (<100 fs, 1 μJ). After interaction with the sample, the probe and signal were directed into a spectrograph (Triax 180, Horiba Jobin Yvon), dispersed using a 1200 or 2400 grooves/mm grating (540 and 400 nm Raman pump, respectively), and detected using a Pixis 100B CCD camera (Princeton Instruments). The steady-state FSRS spectra were averaged for 60 s and the time-resolved FSRS spectra were averaged for 30 s at each time delay. The samples were prepared with an absorbance of 0.5−1 in CD_3CN in a 1 mm quartz cuvette and stirred to limit the effects of heating and sample degradation. The instrument response function for the time-resolved FSRS experiment and the spectral resolution for both FSRS experiments were ∼300 fs and ∼15 cm^{-1}, respectively.

The FSRS spectra were calibrated to the Raman modes of acetone, dichloromethane, and toluene. The electronic baseline was removed by subtracting the resultant fit of the baseline to a cubic polynomial. In the steady-state FSRS spectra, the solvent modes were removed by subtracting the FSRS spectrum of the pure solvent. In the time-resolved FSRS spectra, the solvent and steady-state modes were removed by subtracting the average of the $\Delta t < -1$ ps spectra. The time-resolved FSRS spectra were analyzed by singular value decomposition (SVD)[58] to generate a set of orthonormal basis spectra and a set of corresponding orthogonal vectors containing the time-dependent amplitudes of the basis spectra which were then fit as described above. Additionally, the numerical area and centroid of the transient features were calculated at each time-delay using a home-written program in MATLAB.

Computational Analysis. The geometry optimization of the $PTZ^{+\bullet}$ molecule was performed using Gaussian09[59] at B3LYP[60]/Def2SVP level of theory followed by computation of singlet excited states at TD-CAMB3LYP[61]/ 6-311+G(d,p) level in Q-Chem 5.0.[62] Both calculations were performed in a dielectric continuum model for CH_3CN (SMD[63] for geometry optimization and C-PCM[64] for calculation of excited states). The cationic GS was prepared by removing a beta electron from the neutral species, resulting in an open-shell reference state for TDDFT calculation. Excitation energies were computed from the cationic ground state (GS) using the Tamm−Dancoff approximation[65] (TDA), which is known to reproduce emission and absorption spectra of conjugated molecules with reasonable accuracy. The band shape was simulated using excitation energies and oscillator strengths. While this is not intended to reproduce the vibronic structure of the absorption spectra, the band structure of the unresolved spectrum is well reproduced.[66]

RESULTS

Steady-State Optical Spectroscopy. Ground-state UV−visible absorption spectra of PTZ, PTZ-Per, PTZ-DPA, and PTZ-ACN in CH_2Cl_2 are shown in Figure 1A. The lowest energy absorption band of PTZ occurs at λ = 321 nm (ε = 2600 M^{-1} cm^{-1}), while PTZ-Per, PTZ-DPA, and PTZ-ACN show lowest energy absorption bands at λ = 447 nm (ε = 36 600 M^{-1} cm^{-1}), 400 nm (ε = 13 700 M^{-1} cm^{-1}), and 412 nm (ε = 11 900 M^{-1} cm^{-1}), respectively. A comparison of these low-energy absorption bands with their monomeric reference molecules shows only minimal deviations (Figure S1), which indicates that electronic coupling between the donor and acceptor moieties of the molecules is negligible in the GS.

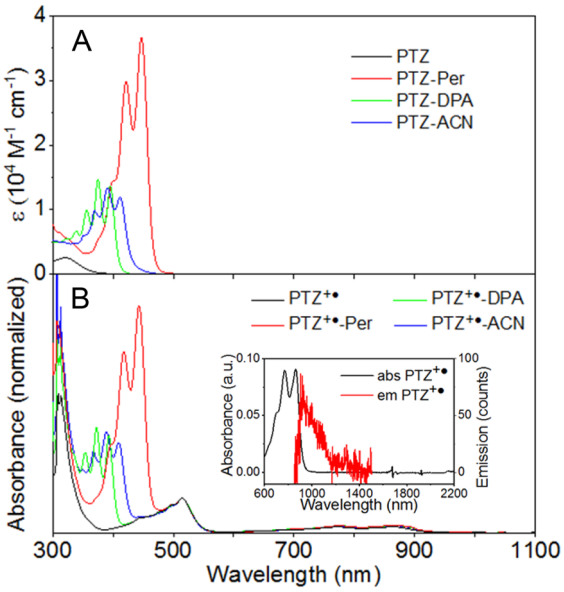

Figure 1. (A) Solution steady-state UV−visible absorption spectra of neutral species in CH_2Cl_2. (B) Solution steady-state absorption spectra of oxidized species in CH_3CN normalized to the λ = 514 nm feature of $PTZ^{+\bullet}$. Inset: Solution steady-state visible-NIR absorption and emission spectra of $PTZ^{+\bullet}$ in CH_3CN.

Steady-state UV−visible absorption spectra of $PTZ^{+\bullet}$, $PTZ^{+\bullet}$-Per, $PTZ^{+\bullet}$-DPA, and $PTZ^{+\bullet}$-ACN in CH_3CN are shown in Figure 1B. The most intense $PTZ^{+\bullet}$ feature appears between λ = 400 and 550 nm with a maximum absorption at λ_{max} = 514 nm. Another broad absorption feature arises between λ = 650 and 900 nm with local maxima at λ_{max} = 772 and 864 nm, which agrees well with the literature.[47] Weak steady-state emission was detected in the NIR from λ = 875 to 1200 nm with a maximum at λ = 924 nm (Figure 1B, inset). The absorption features attributed to $PTZ^{+\bullet}$ in the dyads are unperturbed relative to those of $PTZ^{+\bullet}$ itself, which indicates that the PTZ and the hole donor moieties maintain their electronic isolation upon oxidation of PTZ.

Electrochemistry. Cyclic voltammograms (CV) and differential pulse voltammograms (DPV) of saturated solutions of PTZ and the three dyads in 0.1 M $TBAPF_6$ CH_3CN are shown in Figure 2 and their oxidation potentials summarized in Table 1. PTZ shows a reversible oxidative wave at E_{ox} = 0.70 V vs SCE in the CV, and the reversibility of this wave is maintained in each of the three dyads. The PTZ oxidation potential is only minimally perturbed by introducing the hole acceptors as it is found to be E_{ox} = 0.69 V vs SCE in each dyad. The oxidation

DOI: 10.1021/jacs.8b01778
J. Am. Chem. Soc. 2018, 140, 5290−5299

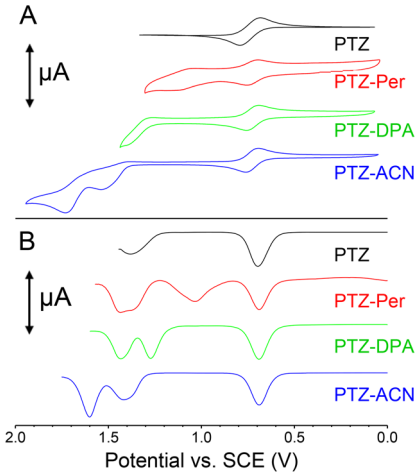

Figure 2. Cyclic voltammograms (A) and differential pulse voltammograms (B) of PTZ (black), PTZ-Per (red), PTZ-DPA (green), and PTZ-ACN (blue) in 0.1 M $TBAPF_6$ in CH_3CN.

Table 1. Redox Potentials (V vs SCE) and estimated ΔG^0_{HT} for Hole Transfer

	E_{OX1}	E_{OX2}	E_{OX3}	ΔG^0_{HT} (eV) D_n	ΔG^0_{HT} (eV) D_1
PTZ	0.70				
PTZ-Per	0.69	1.04		−1.88	−1.04
PTZ-DPA	0.69	1.27		−1.65	−0.81
PTZ-ACN	0.69	1.41	1.60	−1.32	−0.48

potentials of the hole acceptor moieties are E_{ox} = 1.04, 1.27, and 1.60 V vs SCE for PTZ-Per, PTZ-DPA, and PTZ-ACN, respectively. The assignments for these waves were confirmed by comparison of the redox properties of the dyads with their monomeric reference molecules (Figure S2). Although the anthracene monomeric reference molecules show reversible oxidation waves, the PTZ-DPA and PTZ-ACN dyads have irreversible anthracene centered oxidations. The irreversibility of these waves may result from their proximity to the second oxidation of PTZ at E_{ox} = 1.37−1.43 V vs SCE.

Charge-Transfer Energetics. The lowest electronic excited-state energy ($E_{0,0}$ of D_1) can be estimated by averaging the energies of the lowest energy absorptive transition and the highest energy emissive transition.[67] The lowest energy absorption was observed at λ_{max} = 864 nm, and the highest energy emission was observed at λ_{max} = 924 nm, so $E_{0,0}$ of D_1 is 1.39 eV. Thus, the excited-state oxidation potential of D_1 is $E^{ox}_{0,0}$ = ($E_{ox}(PTZ^{+\bullet}/PTZ)$) + $E_{0,0}(PTZ^{+\bullet})$= +2.1 V vs SCE making it a very powerful oxidant. The λ = 514 nm absorption feature is assigned as the $D_n \leftarrow D_0$ transition based on the TDDFT calculations, *vide infra*. The $E_{0,0}$ of D_n is 2.23 eV (λ = 557 nm) based on the red edge of the visible absorption band (Figure 1B), and therefore the excited-state oxidation potential of D_n is $E^{ox}_{0,0}$ = +2.9 V vs SCE.

The Gibbs free energy change for photoinduced hole transfer (ΔG^0_{HT}) in CH_3CN was estimated using eq 1:

$$\Delta G^0_{HT} = (E_{ox}(A^{+\bullet}/A) - E_{ox}(PTZ^{+\bullet}/PTZ)) - E_{0,0}(PTZ^{+\bullet}) \quad (1)$$

where $E_{ox}(A^{+\bullet}/A)$ is the oxidation potential of the hole acceptor of interest, $E_{ox}(PTZ^{+\bullet}/PTZ)$ is the oxidation potential of PTZ, and $E_{0,0}(PTZ^{+\bullet})$ is the doublet excited-state energy of $PTZ^{+\bullet}$. The value of ΔG^0_{HT} for each dyad is summarized in Table 1. Unlike typical estimations of the free energy change for the formation of an ion-pair state using the approximation developed by Weller,[68] Coulombic and solvent reorganization energy considerations are neglected because the charge of the molecule is constant in this charge shift reaction and the fsTA and electrochemical measurements are performed in the same high-polarity solvent (CH_3CN).

Time-Resolved Spectroscopy. The GS recovery dynamics of $PTZ^{+\bullet}$ were investigated using pump−probe fsTA spectroscopy. Figure 3A displays the fsTA spectra at selected time delays following photoexcitation of $PTZ^{+\bullet}$ with a pump pulse centered at λ_{ex} = 517 nm. The data were best fit to an A → B → GS first-order kinetic model with time constants for these processes of $\tau_{A\to B}$ = 10.9 ± 0.4 ps and $\tau_{B\to GS}$ = 32.3 ± 0.8

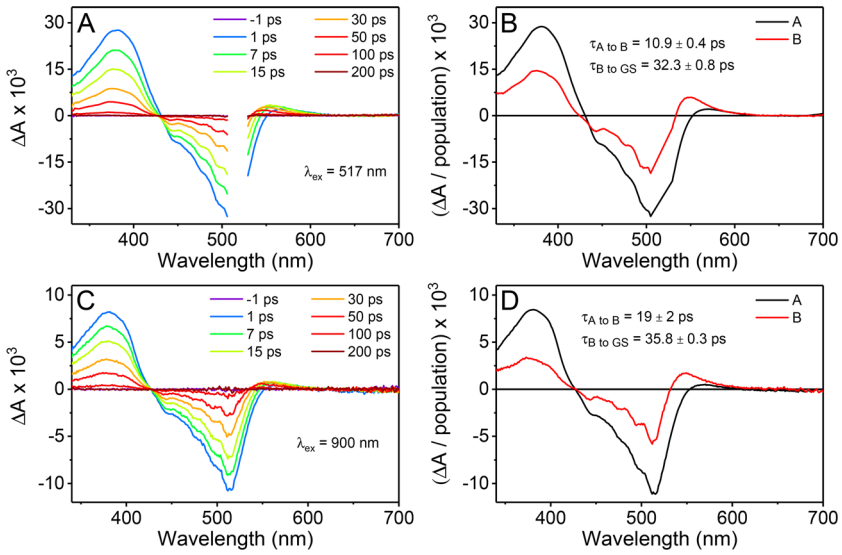

Figure 3. (A,B) λ_{ex} = 517 nm, 1.0 μJ/pulse, CH_3CN. (A) fsTA spectra of $PTZ^{+\bullet}$. (B) Species-associated spectra obtained by global fitting. (C,D) λ_{ex} = 900 nm, 1.0 μJ/pulse, CH_3CN. (C) fsTA spectra of $PTZ^{+\bullet}$. (D) Species-associated spectra obtained by global fitting.

DOI: 10.1021/jacs.8b01778
J. Am. Chem. Soc. 2018, 140, 5290−5299

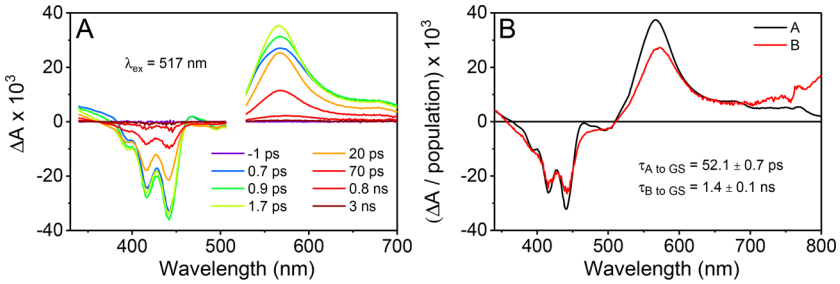

Figure 4. (A) fsTA spectra of PTZ$^{+\bullet}$-Per, λ_{ex} = 517 nm, 1.0 μJ/pulse, CH_3CN. (B) Species-associated spectra obtained by global fitting.

Table 2. Summary of Photophysical Time Constants (ps)

	λ_{ex} = 517 nm			λ_{ex} = 900 nm	
PTZ	$\tau_{A\to B}$	$\tau_{B\to GS}$		$\tau_{A\to B}$	$\tau_{B\to GS}$
	10.9 ± 0.4	32.3 ± 0.8		19 ± 2	35.8 ± 0.3
PTZ-Per	$\tau_{A\to GS}$	$\tau_{B\to GS}$		$\tau_{A\to GS}$	$\tau_{B\to GS}$
	52.1 ± 0.8	1400 ± 100		56 ± 1	1400 ± 100
PTZ-DPA	τ_A	τ_B	τ_C	τ_A	τ_B
	0.9 ± 0.3	4.1 ± 0.3	20 ± 2	0.8 ± 0.3	5.1 ± 0.3
PTZ-ACN	$\tau_{A\to B}$	$\tau_{B\to GS}$	$\tau_{C\to GS}$	$\tau_{A\to B}$	$\tau_{B\to GS}$
	5.3 ± 0.3	20 ± 2	0.4 ± 0.3	6.0 ± 0.3	17.2 ± 0.3

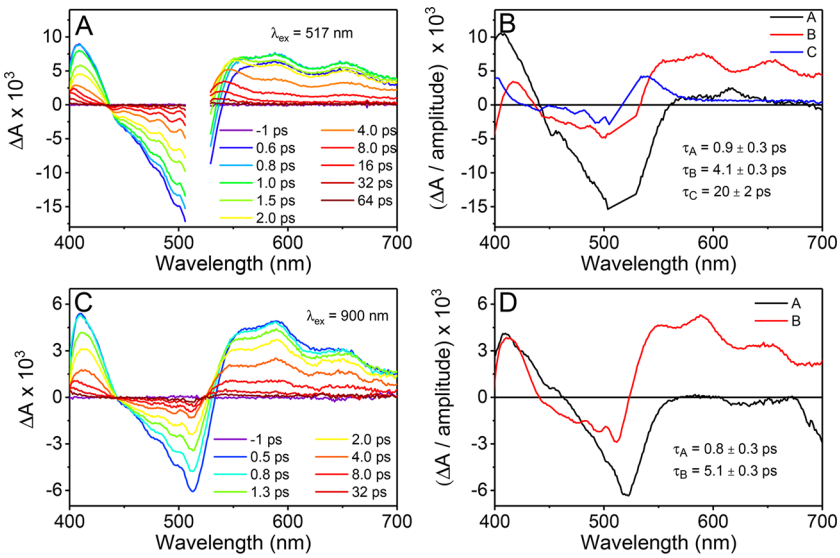

Figure 5. (A,B) λ_{ex} = 517 nm, 1.0 μJ/pulse, CH_3CN. (A) fsTA spectra of PTZ$^{+\bullet}$-DPA. (B) Decay-associated spectra obtained by global fitting. (C,D) λ_{ex} = 900 nm, 1.0 μJ/pulse, CH_3CN. (C) fsTA spectra of PTZ$^{+\bullet}$-DPA. (D) Decay-associated spectra obtained by global fitting.

ps. Analysis of the kinetic fitting and assignments of the spectral features can be found the Supporting Information. The species-associated spectra corresponding to species A and B are shown in Figure 3B. The transient kinetics at selected wavelengths and population dynamics are shown in Figure S3. To further investigate the GS recovery dynamics, PTZ$^{+\bullet}$ was examined following photoexcitation with a pump pulse centered at λ_{ex} = 900 nm (Figure 3C). The species are best fit to the same A → B → GS model; however, the time constants were found to be $\tau_{A\to B}$ = 19 ± 2 ps and $\tau_{B\to GS}$ = 35.8 ± 0.3 ps. The species-associated spectra corresponding to species A and B are shown in Figure 3D. Analysis of the kinetic fitting and assignments of the spectral features can be found the Supporting Information, and the transient kinetics at selected wavelengths and the population dynamics are shown in Figure S5.

The GS recovery dynamics of PTZ$^{+\bullet}$ were also investigated using fsTA with NIR probe wavelengths and FSRS. Following both λ_{ex} = 517 and 900 nm, an excited-state absorption (ESA) at λ_{max} = 1284 nm was observed in the NIR fsTA spectra. The data were fit to the same model as the visible region data, and the time constants extracted were similar (Figures S4 and S6). In the time-resolved FSRS experiment (Figure S18), the Raman pump (λ_{RP} = 400 nm) pulse was selected to be resonant with the stronger ESA at 380 nm to probe the structural dynamics following excitation with λ_{ex} = 517 nm. A single weak transient feature was observed at 1346 cm^{-1} (Figure S18) that exhibits similar decay dynamics as those observed in the fsTA experiments.

Among the three dyads studied, PTZ$^{+\bullet}$-Per has the largest negative ΔG^0_{HT} for hole transfer from ^{2}*PTZ$^{+\bullet}$ to Per, and the dynamics were examined after excitation at both λ_{ex} = 517 and 900 nm. These data were fit to a first-order kinetic model, where species A decays to species B with $\tau_{A\to B} \approx$ 270 ps and to the GS with $\tau_{A\to GS}$ = 52.1 ± 0.8 ps and species B decays to the

DOI: 10.1021/jacs.8b01778
J. Am. Chem. Soc. 2018, 140, 5290−5299

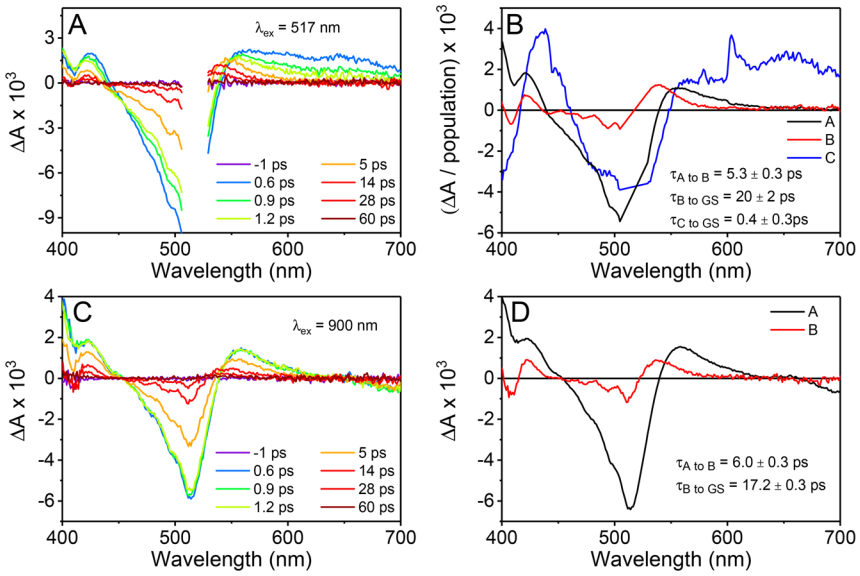

Figure 6. (A,B) λ_{ex} = 517 nm, 1.0 μJ/pulse, CH_3CN. (A) fsTA spectra of $PTZ^{+\bullet}$-ACN. (B) Species-associated spectra obtained by global fitting. (C,D) λ_{ex} = 900 nm, 1.0 μJ/pulse, CH_3CN. (C) fsTA spectra of $PTZ^{+\bullet}$-ACN. (D) Species-associated spectra obtained by global fitting.

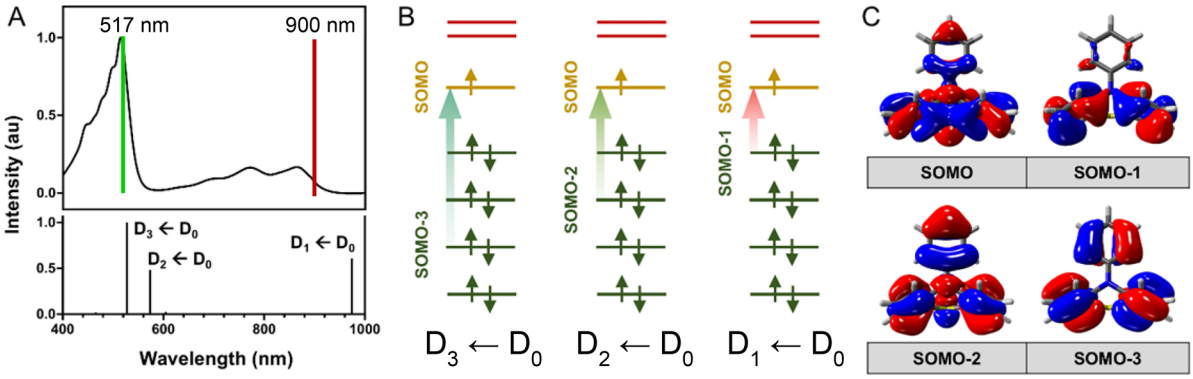

Figure 7. (A) Observed (top) and computed (bottom) UV−vis spectra of $PTZ^{+\bullet}$ with lines indicating the location of the 517 nm (green) and 900 nm (red) excitation pulses. (B) Transitions between MOs corresponding to the relevant transitions. (C) $PTZ^{+\bullet}$ orbitals relevant to optical transitions.

GS with $\tau_{A\rightarrow B}$ = 1.4 ± 0.1 ns (Figure 4; see Supporting Information for details). The transient kinetics at selected wavelengths and population dynamics are shown in Figures S7 and S8. The same model that was used to fit the λ_{ex} = 517 nm data was also used to fit the λ_{ex} = 900 nm data, and the kinetics are essentially unchanged (Table 2). The transient spectra, species-associated spectra, transient kinetics at selected wavelengths, and populations of transient species of $PTZ^{+\bullet}$-Per following excitation at λ_{ex} = 900 nm are shown in Figures S9 and S10.

The hole-transfer reaction ^{2}*$PTZ^{+\bullet}$-DPA → PTZ-$DPA^{+\bullet}$ occurs with ΔG^0_{HT} that is 0.23 eV less negative than that of ^{2}*$PTZ^{+\bullet}$-Per → PTZ-$Per^{+\bullet}$, which causes the hole-transfer dynamics to change. Following excitation at λ_{ex} = 517 nm, the data were globally fit to a sum of three exponentials; the resulting decay-associated spectra are shown in Figure 5B, and the time constants are summarized in Table 2. The transient kinetics at selected wavelengths and amplitude dynamics are shown in Figure S11. Following excitation at λ_{ex} = 900 nm the data were best fit to a sum of two exponentials. Component A has a time constant of τ_A = 0.8 ± 0.3 ps, and component B decays with a time constant of τ_B = 5.1 ± 0.3 ps. Details of the kinetic fitting and assignments of the spectral features can be found the Supporting Information, and the transient kinetics at selected wavelengths and population dynamics are shown in Figure S12.

The hole-transfer reaction ^{2}*$PTZ^{+\bullet}$-ACN → PTZ-$ACN^{+\bullet}$ occurs with ΔG^0_{HT} that is 0.33 eV less negative than that of ^{2}*$PTZ^{+\bullet}$-DPA → PTZ-$DPA^{+\bullet}$, and is the smallest ΔG^0_{HT} in the series, which again results in hole-transfer dynamics that differ from those of $PTZ^{+\bullet}$-Per and $PTZ^{+\bullet}$-DPA (Figure 6). Following excitation at λ_{ex} = 517 nm, the data were best fit using parallel A → B → GS and C → GS kinetics with time constants $\tau_{A\rightarrow B}$ = 5.3 ± 0.3 ps, $\tau_{B\rightarrow GS}$ = 20 ± 2 ps, and $\tau_{C\rightarrow GS}$ = 0.4 ± 0.3 ps. The transient kinetics at selected wavelengths and population dynamics are shown in Figure S14. When the sample was irradiated with a λ_{ex} = 900 nm excitation pulse, the data were best fit to an A → B → GS kinetic model composing of two exponential decays with time constants of $\tau_{A\rightarrow B}$ = 6.0 ± 0.3 ps and $\tau_{B\rightarrow GS}$ = 17.2 ± 0.3 ps. The transient kinetics at selected wavelengths and population dynamics are shown in Figure S15.

DOI: 10.1021/jacs.8b01778
J. Am. Chem. Soc. 2018, 140, 5290−5299

DISCUSSION

The electronic absorption spectrum of $PTZ^{+\bullet}$ was assigned using TDDFT calculations, and a comparison between the experimentally observed and computed UV−visible spectra is shown in Figure 7A and Table 3. Two computed transitions, $D_3 \leftarrow D_0$ and $D_2 \leftarrow D_0$, are likely involved when the sample interacts with the λ_{ex} = 517 nm laser pulse. The combined population of both D_3 and D_2 is referred to as D_n. One computed transition, $D_1 \leftarrow D_0$, is involved when the sample interacts with the λ_{ex} = 900 nm laser pulse. In addition, Figure 7B,C reveals the nature of molecular orbitals (MOs) participating in relevant transitions. It was observed that for both peaks of interest, the transitions are from doubly occupied MOs to the singly occupied MO (SOMO). The SOMO is predominantly located on the twisted 6-membered ring containing the S atom, whereas the originating MOs are delocalized across the aromatic rings.

Table 3. Comparison between Experimentally Observed and Computed Positions of Absorption Maxima of $PTZ^{+\bullet}$

absorption maxima		error	
expt (nm)	theory (nm)	$\lvert E_{expt} - E_{theo}\rvert$ (eV)	%
514	527	0.06	2.5
864	974	0.16	11

Following excitation at both λ_{ex} = 517 and 900 nm, the $PTZ^{+\bullet}$ GS recovery dynamics were fit to the same A → B → GS model, and the species-associated spectra for species A and B are remarkably similar in both cases (Figure 3B,D). Surprisingly, the time constant for the transition from state A to state B nearly doubles when the samples are photoexcited at lower energies (τ = 10.9 ± 0.4 ps for λ_{ex} = 517 nm vs τ = 19 ± 2 ps for λ_{ex} = 900 nm). The electronic absorption and emission spectra of $PTZ^{+\bullet}$ (Figure 1B inset) indicate that the absorption band at λ_{max} = 864 nm is the transition to the lowest energy electronic excited state, and this is supported by the computational analysis. The spectral similarity between species A and species B following either excitation energy, along with the conclusion that the absorption band at λ_{max} = 864 nm is the $D_1 \leftarrow D_0$ electronic transition, suggests that following high-energy excitation (λ_{ex} = 517 nm), internal conversion from the higher electronic state (D_n) to the lowest electronic excited state (D_1) occurs within the instrument response function (IRF), and D_n is not observed in these experiments. The energy gap between D_n and D_1, estimated from the $PTZ^{+\bullet}$ steady-state absorption, is ∼0.9 eV. This matches the wavelength of the ESA absorption maximum observed in the NIR, λ = 1285 nm, 0.96 eV (Figures S4 and S6), which is strong evidence that the NIR ESA is the $D_n \leftarrow D_1$ transition. The NIR data were fit to the same model as the visible data, and the NIR feature decays concomitantly with species A and B, which indicates that both species A and species B are in the lowest electronic excited state, D_1. Following low-energy excitation (λ_{ex} = 900 nm) D_1 is populated directly, and again both species A and species B are observed. Therefore, the observed transition from species A to B in the global fitting analysis is likely a relaxation on the D_1 electronic excited-state potential energy surface ($D_1' \rightarrow D_1$). This model is further supported by the dynamics observed in the time-resolved FSRS experiment. Peak analysis of the 1346 cm^{-1} transient mode, assigned to ring deformation (Figure S18B), suggests a small shift to higher frequency that occurs on a time scale similar to the transition from species A to B while the peak decays on a time scale similar to the decay of species B (Figure S18). The decay of the transient FSRS signal with $\tau \approx$ 35 ps suggests that this process is associated with a transition between electronic states, $D_1 \rightarrow D_0$, which is consistent with the proposed kinetic model. The GS recovery dynamics of $PTZ^{+\bullet}$ are summarized in Figure 8A.

In the case of $PTZ^{+\bullet}$-Per, the hole-transfer dynamics were fit to the same model for both low- and high-energy excitation. This model neglects the initial charge shift reaction $^{2*}PTZ^{+\bullet}$-Per → PTZ-$Per^{+\bullet}$ because the time constant for the charge shift reaction is on the same order as the IRF (∼0.3 ps), and it could not be extracted accurately. This omission is apparent from the deviation of the fit from the data at time delays <1.5 ps (Figures S7−S10). Because the initial hole-transfer occurs within the IRF and no features attributable to $^{2*}PTZ^{+\bullet}$ are observed, we assume that hole transfer occurs from D_n and/or D_1' with unity quantum yield. No hole transfer occurs from D_1 because $D_1' \rightarrow D_1$ relaxation is an order of magnitude slower than the hole-transfer reaction. The reverse charge shift reaction, PTZ-$Per^{+\bullet}$ → $PTZ^{+\bullet}$-Per is modeled using two competing parallel

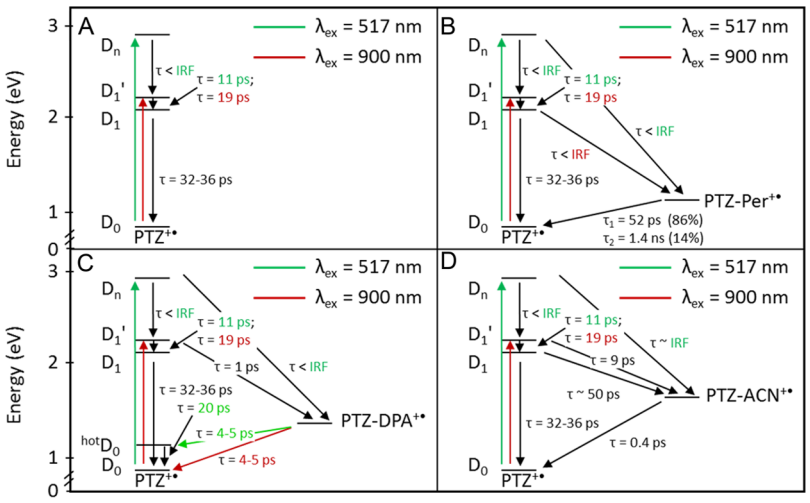

Figure 8. Jablonski diagrams summarizing the photophysics and charge-transfer reactions of (A) $PTZ^{+\bullet}$, (B) $PTZ^{+\bullet}$-Per, (C) $PTZ^{+\bullet}$-DPA, and (D) $PTZ^{+\bullet}$-ACN following excitations at λ_{ex} = 517 nm (green) and λ_{ex} = 900 nm (red).

DOI: 10.1021/jacs.8b01778
J. Am. Chem. Soc. 2018, 140, 5290−5299

processes, each representing different decaying populations of PTZ-Per$^{+\bullet}$. One population of A decays to GS by two sequential first-order processes, A → B → GS, while the other population decays directly to GS, A → GS. We suggest that the two populations of PTZ-Per$^{+\bullet}$ arise from two PTZ conformations. It is well established that PTZ has a nonplanar bowed structure, while PTZ$^{+\bullet}$ is significantly more planar.[47] After the initial excited-state hole-transfer reaction, the neutral PTZ moiety structurally relaxes from its planar to its bowed state. The fact that two decay rates are observed for the reverse hole transfer that re-oxidizes PTZ suggests that there is a competition between back transfer to planar PTZ and structural relaxation to form bowed PTZ. Based on our kinetic analysis (Supporting Information), rapid reverse hole transfer (τ = 52 ps) occurs in 86% of PTZ-Per$^{+\bullet}$ with PTZ remaining in its planar state, while slow hole transfer (τ = 1.4 ns) occurs in 14% of PTZ-Per$^{+\bullet}$ because it is coupled to structural relaxation of PTZ ($\tau \sim$ 270 ps), which increases the nuclear reorganization energy for the reverse hole transfer. We have observed a similar time constant for conformational changes accompanying formation of PTZ$^{+\bullet}$ in PTZ-pyrene dyads.[70] The hole-transfer dynamics for PTZ$^{+\bullet}$-Per are summarized in Figure 8B.

As the hole acceptor becomes more difficult to oxidize, differences between the hole-transfer dynamics following λ_{ex} = 517 and 900 nm excitation become apparent. The transient absorption spectra obtained after excitation of PTZ$^{+\bullet}$-DPA at λ_{ex} = 517 nm were fit to a sum of three exponentials (Table 2), and the corresponding decay-associated spectra are shown in Figure 5B. Component A (Figure 5B, black) clearly consists primarily of PTZ$^{+\bullet}$ ground-state bleach (GSB) and ^{2*}PTZ$^{+\bullet}$ ESA features. This spectrum evolves with the time constant τ_A = 0.9 ± 0.3 ps, which is largely due to the hole-transfer reaction ^{2*}PTZ$^{+\bullet}$(D_1')-DPA → PTZ-DPA$^{+\bullet}$. Component B consists of features attributed to PTZ-DPA$^{+\bullet}$ (Figure 5B, red),[69] which decays back to PTZ$^{+\bullet}$-DPA with τ_B = 4.1 ± 0.3 ps. This is an order of magnitude faster than the decay of PTZ-Per$^{+\bullet}$, and thus greatly out-competes any significant conformational changes in the PTZ moiety. This observation is consistent with both reverse charge shift reactions, PTZ-Per$^{+\bullet}$ → PTZ-Per$^{+\bullet}$ and PTZ-DPA$^{+\bullet}$ → PTZ-DPA$^{+\bullet}$, being in the Marcus normal region of the rate vs free energy of reaction dependence.[71] The relatively low amplitude component C consists of features that are attributed to PTZ$^{+\bullet}$ in a hot ground state ($^{hot}D_0$), which is formed following rapid hole transfer from PTZ-DPA$^{+\bullet}$ back to reform PTZ$^{+\bullet}$-DPA. A positive TA signal is also observed in the NIR fsTA at λ = 917 nm, and this feature also persists at time delays longer than the D_1 NIR ESA feature at λ = 1284 nm (Figure S13A). The presence of positive TA signals bathochromically shifted from each of the ground-state absorbance features suggests the presence of a hot ground state. Therefore, these spectra provide strong evidence suggesting the population of a hot ground state following the reverse hole transfer after high-energy excitation. The PTZ$^{+\bullet}$ $^{hot}D_0$ population decays with τ_C = 20 ± 2 ps (Figure 5B, blue).

When the sample is instead excited at λ_{ex} = 900 nm, the spectra observed can be fit to a sum of two exponential decays. The first decay-associated spectrum again consists primarily of PTZ$^{+\bullet}$ GSB and ^{2*}PTZ$^{+\bullet}$ ESA features, and decays with a time constant of τ_A = 0.8 ± 0.3 ps. The second decay-associated spectrum corresponds to the decay of PTZ-DPA$^{+\bullet}$, and it has a time constant of τ_B = 5.1 ± 0.3 ps. There is no third component corresponding to the PTZ$^{+\bullet}$ ($^{hot}D_0$) decay, presumably because the λ_{ex} = 900 nm excitation pulse provides much less excess energy than the λ_{ex} = 517 nm excitation pulse. Figure 8C summarizes the hole-transfer dynamics of PTZ$^{+\bullet}$-DPA.

Excitation wavelength dependent dynamics are again observed for PTZ$^{+\bullet}$-ACN. The spectra collected for PTZ$^{+\bullet}$-ACN after excitation at λ_{ex} = 517 nm were fit to an A → B → GS, C → GS kinetic model. The spectrum of species A is assigned to ^{2*}PTZ$^{+\bullet}$ (D_1'), and it decays with a time constant of $\tau_{A\to B}$ = 5.3 ± 0.3 ps. This decay is a combination of relaxation to ^{2*}PTZ$^{+\bullet}$ (D_1) and hole transfer to generate PTZ-ACN$^{+\bullet}$. The spectrum of species B is assigned to ^{2*}PTZ$^{+\bullet}$ (D_1), and decays with a time constant of $\tau_{B\to GS}$ = 20 ± 2 ps. The spectrum of species C has a broad feature between λ = 600 and 700 nm, and is assigned to PTZ-ACN$^{+\bullet}$, which decays very rapidly with time constant of $\tau_{C\to GS}$ = 0.4 ± 0.3 ps. Given the short lifetime of PTZ-ACN$^{+\bullet}$, it likely forms by hole transfer from the D_n electronic excited state that is initially populated following the λ_{ex} = 517 nm laser pulse and competes with ultrafast $D_n \to D_1'$ internal conversion. The D_1' electronic state then decays to both D_1 and PTZ-ACN$^{+\bullet}$, but no additional population of PTZ-ACN$^{+\bullet}$ is observed because its rate of formation is slower than the reverse hole transfer from PTZ-ACN$^{+\bullet}$ to form the ground state (inverted kinetics). Again, the decay of D_1 is faster than the corresponding decay observed for ^{2*}PTZ$^{\bullet+}$ (D_1) with no hole acceptor due to a combination of hole transfer from D_1 to form PTZ-ACN$^{\bullet+}$ and internal conversion ($D_1 \to D_0$). Following excitation at λ_{ex} = 900 nm, the data were fit to an A → B → GS kinetic model. The D_1' (species A) and D_1 (species B) electronic excited states are analogous to species A and B following excitation at λ_{ex} = 517 nm, while PTZ-ACN$^{+\bullet}$ is not observed. Given the inverted kinetics for the formation and decay of PTZ-ACN$^{+\bullet}$ produced from D_1' and D_1, an observable population of PTZ-ACN$^{+\bullet}$ never accumulates. The similarity between species A and B after both λ_{ex} = 517 and 900 nm indicates that, unlike PTZ$^{+\bullet}$-DPA, a significant population of $^{hot}D_0$ following the reverse hole transfer does not form in this sample. This is supported by the NIR data, which does not show a feature at λ = 917 nm present at time delays after the decay of the PTZ$^{+\bullet}$ ESA at λ = 1284 (Figure S16). The photoinduced hole-transfer dynamics for PTZ$^{+\bullet}$-ACN are summarized in Figure 8D.

Given the rapid hole-transfer dynamics exhibited by these systems, it will be necessary to increase the lifetime of the oxidized hole acceptor to promote further desirable chemical reactions, such as the delivery of oxidizing equivalents to a catalyst. This can be accomplished readily by applying well-established strategies for modulating charge-transfer rates. For example, decreasing the electronic coupling between PTZ$^{\bullet+}$ and the hole acceptor by extending the length of the spacer group will result in a much longer lived oxidized hole acceptor.[72] Alternatively, utilizing a donor−acceptor triad strategy with two sequential hole-transfer steps will likely increase the lifetime of the oxidized hole acceptor by several orders of magnitude as we have demonstrated for the analogous electron-transfer process initiated by radical anion photoexcitation.[34]

■ CONCLUSIONS

We have demonstrated that ^{2*}PTZ$^{+\bullet}$ can successfully serve as a super-oxidant capable of oxidizing species over a range of oxidation potentials from E_{ox} = 1.04−1.6 V vs SCE. The complex GS recovery dynamics demonstrate the need for a detailed analysis of organic radical ion excited doublet states so that they can provide the energies needed to photosensitize

DOI: 10.1021/jacs.8b01778
J. Am. Chem. Soc. 2018, 140, 5290−5299

catalysts relevant to solar energy and organic synthesis. Currently, our ongoing research is focused on incorporating a $PTZ^{+\bullet}$ photosensitizer into a covalent donor−bridge−acceptor triad to extend the lifetime of the charge-transfer state. We are also interested in identifying additional organic cations that could serve as photosensitizers in energy demanding oxidation reactions.

■ ASSOCIATED CONTENT

Supporting Information

The Supporting Information is available free of charge on the ACS Publications website at DOI: 10.1021/jacs.8b01778.

Experimental details and characterization data (PDF)

■ AUTHOR INFORMATION

Corresponding Author

*m-wasielewski@northwestern.edu

ORCID

Brian T. Phelan: 0000-0002-5849-0319
Atanu Acharya: 0000-0002-6960-7789
Victor S. Batista: 0000-0002-3262-1237
Michael R. Wasielewski: 0000-0003-2920-5440

Notes

The authors declare no competing financial interest.

■ ACKNOWLEDGMENTS

This work was supported by the Chemical Sciences, Geosciences, and Biosciences Division, Office of Basic Energy Sciences, U.S. DOE, under Grant No. DE-FG02-99ER14999 (M.R.W.). Computational resources were provided by Yale HPC and NERSC.

■ REFERENCES

(1) Pao, H.-T.; Tsai, C.-M. *Energy Policy* **2010**, *38*, 7850−7860.
(2) Jafari, T.; Moharreri, E.; Amin, A. S.; Miao, R.; Song, W.; Suib, S. L. *Molecules* **2016**, *21*, 900.
(3) Blankenship, R. E. *Molecular Mechanisms of Photosynthesis*; Blackwell Science: Oxford, 2002.
(4) Hammarström, L. *Acc. Chem. Res.* **2015**, *48*, 840−850.
(5) Favereau, L.; Makhal, A.; Pellegrin, Y.; Blart, E.; Petersson, J.; Goransson, E.; Hammarström, L.; Odobel, F. *J. Am. Chem. Soc.* **2016**, *138*, 3752−3760.
(6) Skaisgirski, M.; Guo, X.; Wenger, O. S. *Inorg. Chem.* **2017**, *56*, 2432−2439.
(7) Kuss-Petermann, M.; Wenger, O. S. *Chem. - Eur. J.* **2017**, *23*, 10808−10814.
(8) Orazietti, M.; Kuss-Petermann, M.; Hamm, P.; Wenger, O. S. *Angew. Chem., Int. Ed.* **2016**, *55*, 9407−9410.
(9) Breslin, D. T.; Fox, M. A. *J. Phys. Chem.* **1993**, *97*, 13341−13347.
(10) Breslin, D. T.; Fox, M. A. *J. Phys. Chem.* **1994**, *98*, 408−411.
(11) Green, S.; Fox, M. A. *J. Phys. Chem.* **1995**, *99*, 14752−14757.
(12) Gumy, J.-C.; Vauthey, E. *J. Phys. Chem. A* **1997**, *101*, 8575−8580.
(13) Brodard, P.; Sarbach, A.; Gumy, J.-C.; Bally, T.; Vauthey, E. *J. Phys. Chem. A* **2001**, *105*, 6594−6601.
(14) Grilj, J.; Laricheva, E. N.; Olivucci, M.; Vauthey, E. *Angew. Chem., Int. Ed.* **2011**, *50*, 4496−4498.
(15) Grilj, J.; Buchgraber, P.; Vauthey, E. *J. Phys. Chem. A* **2012**, *116*, 7516−7522.
(16) Grilj, J.; Zonca, C.; Daku, L. M. L.; Vauthey, E. *Phys. Chem. Chem. Phys.* **2012**, *14*, 6352−8.
(17) Laricheva, E. N.; Olivucci, M.; Grilj, J.; Vauthey, E. Subpicosecond Excited-State Decay of Wurster's Blue Revealed by Ultrafast Spectroscopy and Explained by Quantum Chemistry. *Abstracts of Papers, 243rd ACS National Meeting & Exposition*, San Diego, CA, March 25−29, 2012; COMP-461.
(18) Englman, R.; Jortner, J. *Mol. Phys.* **1970**, *18*, 145−164.
(19) Tokmachev, A. M.; Boggio-Pasqua, M.; Bearpark, M. J.; Robb, M. A. *J. Phys. Chem. A* **2008**, *112*, 10881−10886.
(20) Gosztola, D.; Niemczyk, M. P.; Svec, W.; Lukas, A. S.; Wasielewski, M. R. *J. Phys. Chem. A* **2000**, *104*, 6545−6551.
(21) Lukas, A. S.; Miller, S. E.; Wasielewski, M. R. *J. Phys. Chem. B* **2000**, *104*, 931−940.
(22) Lukas, A. S.; Bushard, P. J.; Wasielewski, M. R. *J. Am. Chem. Soc.* **2001**, *123*, 2440−2441.
(23) Ghosh, I.; Ghosh, T.; Bardagi, J. I.; Koenig, B. *Science* **2014**, *346*, 725−728.
(24) Fujitsuka, M.; Kim, S. S.; Lu, C.; Tojo, S.; Majima, T. *J. Phys. Chem. B* **2015**, *119*, 7275−7282.
(25) Zeng, L.; Liu, T.; He, C.; Shi, D.; Zhang, F.; Duan, C. *J. Am. Chem. Soc.* **2016**, *138*, 3958−3961.
(26) Lu, C.; Fujitsuka, M.; Sugimoto, A.; Majima, T. *J. Phys. Chem. C* **2016**, *120*, 12734−12741.
(27) Lu, C.; Fujitsuka, M.; Sugimoto, A.; Majima, T. *J. Phys. Chem. C* **2017**, DOI: 10.1021/acs.jpcc.7b10926.
(28) Lu, C.; Fujitsuka, M.; Sugimoto, A.; Majima, T. *J. Phys. Chem. C* **2017**, *121*, 4558−4563.
(29) Lu, C.; Fujitsuka, M.; Majima, T. *J. Phys. Chem. C* **2017**, *121*, 649−655.
(30) Fujitsuka, M.; Majima, T. *J. Photochem. Photobiol., C* **2018**, *35*, 25−37.
(31) Kobr, L.; Gardner, D. M.; Smeigh, A. L.; Dyar, S. M.; Karlen, S. D.; Carmieli, R.; Wasielewski, M. R. *J. Am. Chem. Soc.* **2012**, *134*, 12430−12433.
(32) Krzyaniak, M. D.; Kobr, L.; Rugg, B. K.; Phelan, B. T.; Margulies, E. A.; Nelson, J. N.; Young, R. M.; Wasielewski, M. R. *J. Mater. Chem. C* **2015**, *3*, 7962−7967.
(33) La Porte, N. T.; Martinez, J. F.; Hedstrom, S.; Rudshteyn, B.; Phelan, B. T.; Mauck, C. M.; Young, R. M.; Batista, V. S.; Wasielewski, M. R. *Chem. Sci.* **2017**, *8*, 3821−3831.
(34) Martinez, J. F.; La Porte, N. T.; Mauck, C. M.; Wasielewski, M. R. *Faraday Discuss.* **2017**, *198*, 235−249.
(35) Hedstrom, S.; Chaudhuri, S.; La Porte, N. T.; Rudshteyn, B.; Martinez, J. F.; Wasielewski, M. R.; Batista, V. S. *J. Am. Chem. Soc.* **2017**, *139*, 16466−16469.
(36) Martinez, J. F.; La Porte, N. T.; Wasielewski, M. R. *J. Phys. Chem. C* **2018**, *122*, 2608−2617.
(37) Johnston, L. J. *Chem. Rev.* **1993**, *93*, 251−266.
(38) Shida, T. *Electronic Absorption Spectra of Radical Ions*; Elsevier: New York, 1988.
(39) Gosztola, D.; Niemczyk, M. P.; Wasielewski, M. R. *J. Am. Chem. Soc.* **1998**, *120*, 5118−5119.
(40) Soni, D.; Gangada, S.; Duvva, N.; Roy, T. K.; Nimesh, S.; Arya, G.; Giribabu, L.; Chitta, R. *New J. Chem.* **2017**, *41*, 5322−5333.
(41) Antony, M. P.; Moehl, T.; Wielopolski, M.; Moser, J. E.; Nair, S.; Yu, Y. J.; Kim, J. H.; Kay, K. Y.; Jung, Y. S.; Yoon, K. B.; Grätzel, C.; Zakeeruddin, S. M.; Grätzel, M. *ChemSusChem* **2015**, *8*, 3859−3868.
(42) Govindarajan, S.; Gao, S.; Cai, W.; Yam, C. *Mol. Phys.* **2017**, *115*, 731−742.
(43) Lian, S.; Weinberg, D. J.; Harris, R. D.; Kodaimati, M. S.; Weiss, E. A. *ACS Nano* **2016**, *10*, 6372−6382.
(44) Guo, J.; Li, X.-L.; Nie, H.; Luo, W.; Hu, R.; Qin, A.; Zhao, Z.; Su, S.-J.; Tang, B. Z. *Chem. Mater.* **2017**, *29*, 3623−3631.
(45) Daub, J.; Beck, M.; Knorr, A.; Spreitzer, H. *Pure Appl. Chem.* **1996**, *68*, 1399−1404.
(46) Hsieh, T.-S.; Wu, J.-Y.; Chang, C.-C. *Dyes Pigm.* **2015**, *112*, 34−41.
(47) Sun, D.; Rosokha, S. V.; Kochi, J. K. *J. Am. Chem. Soc.* **2004**, *126*, 1388−1401.
(48) Okada, K.; Imakura, T.; Oda, M.; Murai, H.; Baumgarten, M. *J. Am. Chem. Soc.* **1996**, *118*, 3047−8.
(49) Wang, X.; Zhang, Z.; Song, Y.; Su, Y.; Wang, X. *Chem. Commun.* **2015**, *51*, 11822−11825.

DOI: 10.1021/jacs.8b01778
J. Am. Chem. Soc. 2018, 140, 5290−5299

(50) McCamant, D. W.; Kukura, P.; Yoon, S.; Mathies, R. A. *Rev. Sci. Instrum.* **2004**, *75*, 4971−4980.
(51) Yao, L.; Pan, Y.; Tang, X.; Bai, Q.; Shen, F.; Li, F.; Lu, P.; Yang, B.; Ma, Y. *J. Phys. Chem. C* **2015**, *119*, 17800−17808.
(52) Li, D.; Ren, J.; Li, J.; Wang, Z.; Bo, G. *Dyes Pigm.* **2001**, *49*, 181−186.
(53) Brown, K. E.; Veldkamp, B. S.; Co, D. T.; Wasielewski, M. R. *J. Phys. Chem. Lett.* **2012**, *3*, 2362−2366.
(54) Goldsmith, R. H.; DeLeon, O.; Wilson, T. M.; Finkelstein-Shapiro, D.; Ratner, M. A.; Wasielewski, M. R. *J. Phys. Chem. A* **2008**, *112*, 4410−4414.
(55) Connelly, N. G.; Geiger, W. E. *Chem. Rev.* **1996**, *96*, 877−910.
(56) Young, R. M.; Dyar, S. M.; Barnes, J. C.; Juricek, M.; Stoddart, J. F.; Co, D. T.; Wasielewski, M. R. *J. Phys. Chem. A* **2013**, *117*, 12438−12448.
(57) *MATLAB*; The Mathworks, Inc.: Natick, MA, 2013.
(58) Henry, E.; Hofrichter, J. *Methods Enzymol.* **1992**, *210*, 129−192.
(59) Frisch, M.; Trucks, G. W.; Schlegel, H. B.; Scuseria, G. E.; Robb, M. A.; Cheeseman, J. R.; Scalmani, G.; Barone, V.; Mennucci, B.; Petersson, G. A.; et al. *Gaussian 09*, revision A.02; Gaussian, Inc.: Wallingford, CT, 2009.
(60) Becke, A. D. *J. Chem. Phys.* **1993**, *98*, 5648−5652.
(61) Yanai, T.; Tew, D. P.; Handy, N. C. *Chem. Phys. Lett.* **2004**, *393*, 51−57.
(62) Shao, Y.; Gan, Z.; Epifanovsky, E.; Gilbert, A. T. B.; Wormit, M.; Kussmann, J.; Lange, A. W.; Behn, A.; Deng, J.; Feng, X.; Ghosh, D.; Goldey, M.; Horn, P. R.; Jacobson, L. D.; Kaliman, I.; Khaliullin, R. Z.; Kus, T.; Landau, A.; Liu, J.; Proynov, E. I.; Rhee, Y. M.; Richard, R. M.; Rohrdanz, M. A.; Steele, R. P.; Sundstrom, E. J.; Woodcock, H. L.; Zimmerman, P. M.; Zuev, D.; Albrecht, B.; Alguire, E.; Austin, B.; Beran, G. J. O.; Bernard, Y. A.; Berquist, E.; Brandhorst, K.; Bravaya, K. B.; Brown, S. T.; Casanova, D.; Chang, C. M.; Chen, Y.; Chien, S. H.; Closser, K. D.; Crittenden, D. L.; Diedenhofen, M.; DiStasio, R. J.; Do, H.; Dutoi, A. D.; Edgar, R. G.; Fatehi, S.; Fusti-Molnar, L.; Ghysels, A.; Golubeva-Zadorozhnaya, A.; Gomes, J.; Hanson-Heine, M. W. D.; Harbach, P. H. P.; Hauser, A. W.; Hohenstein, E. G.; Holden, Z. C.; Jagau, T. C.; Ji, H.; Kaduk, B.; Khistyaev, K.; Kim, J.; Kim, J.; King, R. A.; Klunzinger, P.; Kosenkov, D.; Kowalczyk, T.; Krauter, C. M.; Lao, K. U.; Laurent, A.; Lawler, K. V.; Levchenko, S. V.; Lin, C. Y.; Liu, F.; Livshits, E.; Lochan, R. C.; Luenser, A.; Manohar, P.; Manzer, S. F.; Mao, S. P.; Mardirossian, N.; Marenich, A. V.; Maurer, S. A.; Mayhall, N. J.; Neuscamman, E.; Oana, C. M.; Olivares-Amaya, R.; O'Neill, D. P.; Parkhill, J. A.; Perrine, T. M.; Peverati, R.; Prociuk, A.; Rehn, D. R.; Rosta, E.; Russ, N. J.; Sharada, S. M.; Sharma, S.; Small, D. W.; Sodt, A.; Stein, T.; Stuck, D.; Su, Y. C.; Thom, A. J. W.; Tsuchimochi, T.; Vanovschi, V.; Vogt, L.; Vydrov, O.; Wang, T.; Watson, M. A.; Wenzel, J.; White, A.; Williams, C. F.; Yang, J.; Yeganeh, S.; Yost, S. R.; You, Z. Q.; Zhang, I. Y.; Zhang, X.; Zhao, Y.; Brooks, B. R.; Chan, G. K. L.; Chipman, D. M.; Cramer, C. J.; Goddard, W. A.; Gordon, M. S.; Hehre, W. J.; Klamt, A.; Schaefer, H. F.; Schmidt, M. W.; Sherrill, C. D.; Truhlar, D. G.; Warshel, A.; Xu, X.; Aspuru-Guzik, A.; Baer, R.; Bell, A. T.; Besley, N. A.; Chai, J. D.; Dreuw, A.; Dunietz, B. D.; Furlani, T. R.; Gwaltney, S. R.; Hsu, C. P.; Jung, Y.; Kong, J.; Lambrecht, D. S.; Liang, W.; Ochsenfeld, C.; Rassolov, V. A.; Slipchenko, L. V.; Subotnik, J. E.; Van Voorhis, T.; Herbert, J. M.; Krylov, A. I.; Gill, P. M. W.; Head-Gordon, M. *Mol. Phys.* **2015**, *113*, 184−215.
(63) Marenich, A. V.; Cramer, C. J.; Truhlar, D. G. *J. Phys. Chem. B* **2009**, *113*, 6378−6396.
(64) Cossi, M.; Rega, N.; Scalmani, G.; Barone, V. *J. Comput. Chem.* **2003**, *24*, 669−681.
(65) Hirata, S.; Head-Gordon, M. *Chem. Phys. Lett.* **1999**, *314*, 291−299.
(66) Marenich, A. V.; Cramer, C. J.; Truhlar, D. G. *J. Phys. Chem. B* **2015**, *119*, 958−967.
(67) Veldkamp, B. S.; Han, W.-S.; Dyar, S. M.; Eaton, S. W.; Ratner, M. A.; Wasielewski, M. R. *Energy Environ. Sci.* **2013**, *6*, 1917−1928.
(68) Weller, A. *Z. Phys. Chem.* **1982**, *133*, 93.
(69) Sioda, R. E. *J. Phys. Chem.* **1968**, *72*, 2322−2330.
(70) Daub, J.; Engl, R.; Kurzawa, J.; Miller, S. E.; Schneider, S.; Stockmann, A.; Wasielewski, M. R. *J. Phys. Chem. A* **2001**, *105*, 5655−5665.
(71) Marcus, R. A. *J. Chem. Phys.* **1956**, *24*, 966−978.
(72) Scott, A. M.; Miura, T.; Ricks, A. B.; Dance, Z. E. X.; Giacobbe, E. M.; Colvin, M. T.; Wasielewski, M. R. *J. Am. Chem. Soc.* **2009**, *131*, 17655−17666.

DOI: 10.1021/jacs.8b01778
J. Am. Chem. Soc. 2018, 140, 5290−5299